

Effect of the magnetization parameter on electron acceleration during relativistic magnetic reconnection in ultra-intense laser-produced plasma

Qian Zhang(张茜), Yongli Ping(平永利), Weiming An(安维明), Wei Sun(孙伟), and Jiayong Zhong(仲佳勇)
Citation: Chin. Phys. B, 2022, 31 (**6**): 065203. DOI: 10.1088/1674-1056/ac3397
Journal homepage: http://cpb.iphy.ac.cn; http://iopscience.iop.org/cpb

What follows is a list of articles you may be interested in

Electron acceleration during magnetic islands coalescence and division process in a guide field reconnection

Shengxing Han(韩圣星), Huanyu Wang(王焕宇), and Xinliang Gao(高新亮)
Chin. Phys. B, 2022, 31 (**2**): 025202. DOI: 10.1088/1674-1056/ac21c0

Spontaneous growth of the reconnection electric field during magnetic reconnection with a guide field: A theoretical model and particle-in-cell simulations

Kai Huang(黄楷), Quan-Ming Lu(陆全明), Rong-Sheng Wang(王荣生), Shui Wang(王水)
Chin. Phys. B, 2020, 29 (**7**): 075202. DOI: 10.1088/1674-1056/ab8da0

Basic features of the multiscale interaction between tearing modes and slab ion-temperature-gradient modes

L Wei(魏来), Z X Wang(王正汹), J Q Li(李继全), Z Q Hu(胡朝清), Y Kishimoto(岸本泰明)
Chin. Phys. B, 2019, 28 (**12**): 125203. DOI: 10.1088/1674-1056/ab5437

Formation of electron depletion layer and parallel electric field in the separatrix region of anti-parallel magnetic reconnection

Zisheng Li(李子圣), Huanyu Wang(王焕宇), Xinliang Gao(高新亮)
Chin. Phys. B, 2019, 28 (**7**): 075203. DOI: 10.1088/1674-1056/28/7/075203

Out-of-plane shear flow effects on fast magnetic reconnection in a two-dimensional hybrid simulation model

Wang Lin, Wang Xian-Qu, Wang Xiao-Gang, Liu Yue
Chin. Phys. B, 2014, 23 (**2**): 025203. DOI: 10.1088/1674-1056/23/2/025203

Effect of the magnetization parameter on electron acceleration during relativistic magnetic reconnection in ultra-intense laser-produced plasma

Qian Zhang(张茜)[1,2], Yongli Ping(平永利)[1,2,†], Weiming An(安维明)[1], Wei Sun(孙伟)[1], and Jiayong Zhong(仲佳勇)[1,‡]

[1] *Department of Astronomy, Beijing Normal University, Beijing* 100875, *China*

[2] *CAS Key Laboratory of Geospace Environment, University of Science & Technology of China, Hefei* 230026, *China*

(Received 3 August 2021; revised manuscript received 5 October 2021; accepted manuscript online 27 October 2021)

Relativistic magnetic reconnection (MR) driven by two ultra-intense lasers with different spot separation distances is simulated by a three-dimensional (3D) kinetic relativistic particle-in-cell (PIC) code. We find that changing the separation distance between two laser spots can lead to different magnetization parameters of the laser plasma environment. As the separation distance becomes larger, the magnetization parameter σ becomes smaller. The electrons are accelerated in these MR processes and their energy spectra can be fitted with double power-law spectra whose index will increase with increasing separation distance. Moreover, the collisionless shocks' contribution to energetic electrons is close to the magnetic reconnection contribution with σ decreasing, which results in a steeper electron energy spectrum. Basing on the 3D outflow momentum configuration, the energetic electron spectra are recounted and their spectrum index is close to 1 in these three cases because the magnetization parameter σ is very high in the 3D outflow area.

Keywords: collisionless shocks, magnetic reconnection, magnetization parameter, electron acceleration

PACS: 52.50.Lp, 94.30.cp, 52.38.Fz **DOI:** 10.1088/1674-1056/ac3397

1. Introduction

There are a number of particle acceleration processes involved in astrophysical phenomena such as gamma ray bursts, jets from active galactic nuclei, and cosmic rays from the super-nova remnants.[1–5] Two of these processes are magnetic reconnection (MR) and collisionless shocks (CSs). Both of these processes lead to the acceleration of charged particles and will be discussed in this work. MR, for example, leads to the conversion of magnetic energy to kinetic energy. In the heliosphere, the current sheet formed by the interaction between the solar wind and the geomagnetic field is also considered as a region where magnetic fields reconnect, and thus energy conversion and dissipation occur.[6] Energetic particles accelerated by MR and/or CS have also been observed in the laboratory.

In the laboratory, the use of nanosecond lasers focused on plastic or metal targets produces a warm dense plasma and a mega-Gauss (MG) magnetic field due to the Biermann battery effect, which is similar to the astrophysical environment.[7,8] Key features of MR have been found in plasmas generated by the interaction of two laser beams with a target, including the MR structure and two high-velocity collimated jets in the reconnection layer.[9,10] The MR-induced ring top x-ray source and outflow/jet in solar flares were first simulated in the laboratory using MG magnetic field generated by the interaction of a high-intensity laser with a target. In addition, the decoupling of ions and electrons at the length of the ion inertia of the diffusion region has been determined.[11] Electrons are accelerated to relativistic velocity driven by MR in the laboratory.[12–17] The pre-magnetized plasma CS front increases the reflection of particles on the shock surface before the collision of the two plasmas to form magnetic reconnection.[18] Electrons are effectively accelerated to relativistic non-thermal energy in the small-scale turbulence generated by shock by first-order Fermi acceleration.[19] In our work we will employ particle-in-cell (PIC) simulation methods; such methods have previously been used in comprehensive studies of high-energy-density plasmas and MR.[20–23] The high-energy electrons were accelerated and injected in the reconnection zone.[24] It is found that the electron "pick-up ring" and the electrons accelerated by MR have a flatter spectrum compared with single laser and target interaction.[25]

The energy spectrum index is an important parameter of reaction electron acceleration efficiency.[26,27] In the relativistic MR regime, a large number of studies have shown that the electron energy spectrum index p approaches 1, where the distribution of the electron energy is $N(\gamma) = C\gamma^{-p}$ and C is a constant.[28] The acceleration driven by the reconnection electric field is so intense that the power-law index of the non-thermal particle energy spectrum tail is close to 1.[29–31] For relativistic MR, the magnetization parameter $\sigma = B^2/(\mu_0 n_e m_e c^2)$ is usually much larger than 1,[32] where σ is the ratio of the energy density in reconnecting the magnetic field to the rest mass energy density and n_e is the electron den-

†Corresponding author. E-mail: ylping@bnu.edu.cn

‡Corresponding author. E-mail: jyzhong@bnu.edu.cn

© 2022 Chinese Physical Society and IOP Publishing Ltd

sity.

In this paper, we present 3D PIC simulation results for relativistic MR driven by two ultra-intense lasers with different spot separation distance. The purpose of our simulation is to obtain the changing plasma environment (magnetization parameter σ) in the reconnection region with a variable separation of the laser spots and to study the influence of electron acceleration in different plasma environments. The simulation results show that the magnetization parameter in the reconnection region will increase when the distance between the two laser spots decreases. Because a larger magnetization parameter represents stronger magnetic energy, particles can be efficiently accelerated by MR and have a higher reconnection rate. It is found that CS plays an important role in electron acceleration in MR driven by ultra-intense lasers. Lastly, the 3D momentum configuration is presented.

2. Simulation and setup

We used KLAP, which is a PIC code used to study energetic particle acceleration under ultra-intense laser and plasma interactions.[33,34] In a previous simulation of MR, electrons with relativistic energies were generated in the MR process via an ultra-intense laser–plasma interaction.[25] In this paper, the relativistic MR process driven by two ultra-intense lasers with different spot separation distance is simulated. The simulation box size was $L_x \times L_y \times L_z = 30\ \mu\text{m} \times 24\ \mu\text{m} \times 50\ \mu\text{m}$, which was divided into $600 \times 480 \times 1000$ cells. The number of particles per cell was 8 and there were more than 2.3 billion particles in total. Both particles and fields had periodic boundary conditions in the x and y directions, and radiating boundary conditions in the z direction.

Initially, two identical circularly polarized laser pulses were injected into the plasma target along the z direction. Two laser pulses had a peak intensity of 5×10^{20} W/cm^2, with a 3 μm spot diameter size. The wavelength of the laser was $\lambda_0 = 1\ \mu\text{m}$, and its period was $T_0 = \lambda/c \approx 3.33$ fs. The normalized laser vector potential was $a_0 = 13.5$. So, the upstream side of the MR region showed the bulk Lorentz factor of $\gamma_0 = (1 + a_0^2)^{1/2} = 13.5$. The initial electron and ion temperatures were 10 keV and 0.01 keV respectively. The Debye length was $\lambda_D = (kT_e/\mu_0 n_e e^2)^{1/2} \approx 0.235\ \mu\text{m} \approx 4.7L$ ($L = 0.05\ \mu\text{m}$ is the cell size in the simulation box). The electron skin depth was $d_e = c/\omega_{pe} \approx 0.71\ \mu\text{m}$, where $\omega_{pe} = (\mu_0 e^2 n_0/\gamma_0 m_e)^{1/2}$ is the electron plasma frequency. In addition, d_e is close to the laser wavelength λ_0. Throughout this paper we set the laser frequency to $f = c/\lambda$, and we use the normal value of the mass ratio of a proton to an electron: $m_p/m_e = 1836$. In this paper, we normalize the magnetic field, the electric field and the electron density to $B_0 = (I/\varepsilon c)^{1/2}/c = 1.45 \times 10^5 T$, $E_0 = 4.34 \times 10^{13}$ V/m, $n_0 = n_c = m_e\omega_0^2/\mu_0 e^2 = 1.15 \times 10^{21}$ cm^{-3}, respectively, where n_c is the critical plasma density.

The initial plasma density in the simulation box had a varying profile along the z direction

$$n(z) = \begin{cases} (z - z_0)/z_0, & 5\ \mu\text{m} < z < 10\ \mu\text{m}, \\ 1, & 10\ \mu\text{m} < z < 15\ \mu\text{m}, \\ (1 - (z - z_1)/L_0), & 15\ \mu\text{m} < z < 35\ \mu\text{m}, \\ 0, & \text{otherwise}, \end{cases} \tag{1}$$

where $z_0 = 5\ \mu\text{m}$, $z_1 = 15\ \mu\text{m}$, and $L_0 = 20\ \mu\text{m}$.

Figure 1 shows the evolution of the reconnection rate $E_z/V_{Ae}B_A$ versus time, where E_z are the electric fields in the reconnection points (X-point) versus time. V_{Ae} is the velocity of Alfvén and B_A is the asymptotic magnetic field strength at the time of the maximum reconnection field. With the laser separation distance of d_s of 8 μm (black solid line) in case A, the reconnection rate is almost zero between $20T_0$ and $35T_0$, and MR does not occur. The reconnection rate increases from $40T_0$ and reaches its maximum 0.28 at $t = 50T_0$; then the reconnection rate starts to go down. For the cases with a laser separation distance of 9 μm (red dashed line) in case B and 10 μm (blue dotted line) in case C, the reconnecting rates reach their maximum, 0.37 and 0.49, at $t = 55T_0$, respectively. The reconnection rate increases with increasing spots separation distance, which means that the magnetic energy dissipates faster in the corresponding reconnection region. The evolution trend of the reconnection rate with the separation distance is consistent with the formula[35]

$$R_t = 2.122 \times 10^4 \sqrt{\frac{d_r}{\sqrt{I_0}}}, \tag{2}$$

where d_r describes the distance of the laser spot to the reconnection point and I_0 is the laser peak intensity. At $t = 75T_0$, there is a second bump in the reconnecting rate.

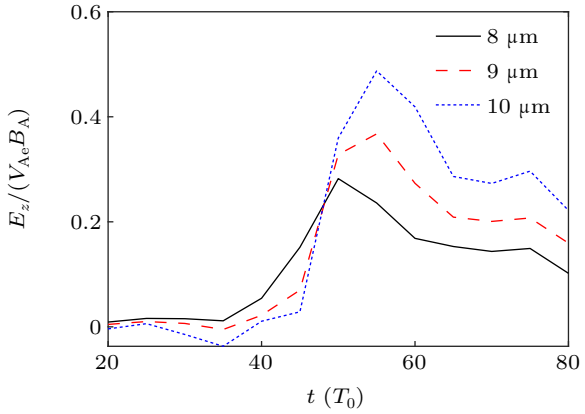


Fig. 1. The reconnection rates for the lasers' separation with 8 μm (black solid line) in case A, 9 μm (red dashed line) in case B and 10 μm (blue dotted line) in case C are $50T_0$, $55T_0$ and $55T_0$, respectively, where the electric field is normalized by $E_z/V_{Ae}B_A$.

3. Electron acceleration in magnetic reconnection with different separation distances

When two laser beams are injected into a plasma target with near-critical density, the laser will push the electrons for-

ward and generate a co-directional current and a quasi-static in-plane magnetic field. The anti-parallel magnetic fields encounter each other and MR occurs in the middle of the two lasers, as shown enclosed by the white dotted rectangle in Figs. 2(a) and (b). Relativistic energetic electrons are generated through the interaction between the high-power ultrashort femetosecond laser pulses and the target. According to a previous study, the current layer of the MR driven by ultra-intense lasers is smaller than the ion scale (ion skin depth).[35] This means that the electrons are frozen with the magnetic field line and move towards one another. Therefore, this MR process happens in the electron diffusion region (EDR).

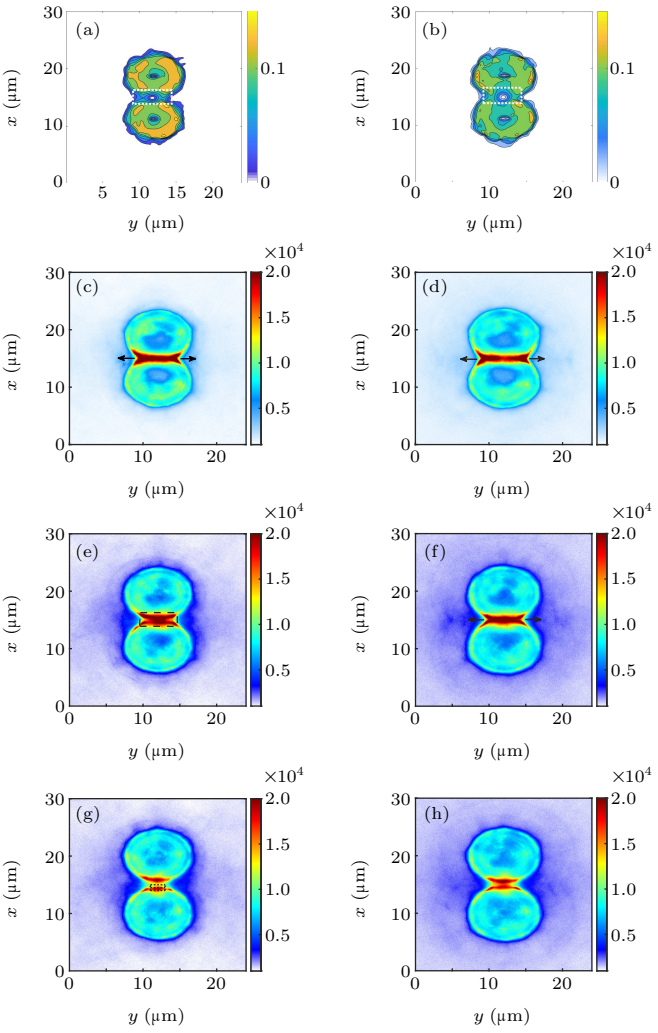


Fig. 2. The in-plane magnetic field $|B_\perp|$ for case A is on the x–y plane with $z = 20$ μm at $t = 50T_0$ (a) and $55T_0$ (b), where the magnetic fields are normalized by the initial laser $B_0 = 1.45 \times 10^5$ T. The electron energy density distributions (electron energy in the range of $3 < \gamma_e < 20$) for case A [(c),(d)], case B [(e),(f)], and case C [(g),(h)] are at $t = 50T_0$ (left column) and $55T_0$ (right column), respectively.

Figures 2(c)–2(h) show the electron energy density distribution electron energy in the range of $(3 < \gamma_e < 20)$ along the z direction at $t = 50T_0$ and $55T_0$. It clearly shows that there are high-density electrons in the reconnection region and outflow region, where the black arrow points the outflow direction. In case A, a large number of the energetic particles are accelerated by the reconnection field of MR in the central X-line, where the dissipated magnetic energy is converted into electron kinetic energy. The larger the separation of the two laser spots, the fewer the high-energy particles accelerated at the magnetic energy dissipation area. However, we find that a large number of electrons have been accelerated to the high-energy state when two magnetic tubes compress each other before MR occurs, possibly due to magnetic pressure or/and CS (Fermi-like acceleration) as Lu *et al.* presented.[21] As shown in Fig. 2(g), more energetic electrons pile up to create a double-layer structure at the compressing magnetic rings, near the X-line region in the bottom of Fig. 2(g), shown in black dotted rectangle. At $t = 55T_0$, this double-layer structure still exists, as seen in Fig. 2(h).

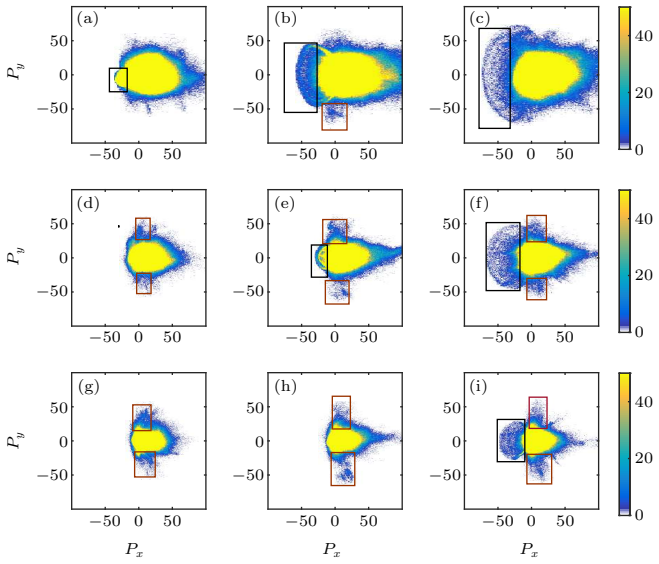


Fig. 3. Electron distribution in the phase space of (p_z, p_y). From top to bottom, the rows correspond to case A, B, and C. From left to right, the columns correspond to $45T_0$, $50T_0$, and $55T_0$, in chronological order.

In order to study electron acceleration by MR, we select the electrons in the volume of 14 μm $< x <$ 16 μm, 7 μm $< y <$ 17 μm, and 10 μm $< z <$ 25 μm from $t = 45T_0$ to $55T_0$, where the current sheet is located. In the previous work, we found there is a bubble (which is in the black rectangle) in the electron momentum distribution of p_z–p_y, which is called the pick-up ring.[25] As shown in Figs. 3(c)–3(i), the smaller the lasers' separation distance is, the larger the "pick-up ring". The reconnection electric field is $E_z = 0.037$, 0.032, and 0.028 in case A, B, and C, respectively. When the separation distance between the two lasers becomes smaller, the reconnection electric field becomes stronger and more electrons will be accelerated to higher energy along the z direction in our simulation and induce a larger pick-up ring.

Figure 4 shows the electron energy spectra in the reconnection region of case A, case B, and case C driven by two lasers with MR (shown as the black line) corresponding to a single laser case without MR (shown as the blue line). In the

range of $\gamma_0 < \gamma_e < 50$, the electron energy spectrum is fit as a power-law distribution and its spectrum indexes are $p_2 = 2.5$, 3.0, and 3.2 in case A, B, C respectively as the pink dotted lines shown in Figs. 4(a)–4(c), which are as the same as the spectrum indexes obtained by single laser driving. Compared with the energy spectrum generated by the interaction of the single-sided laser and target, the range of the power-law spectrum with the same index is wider than that generated by the interaction of two lasers and plasma. With the increase of the laser separation distance, fewer electrons are accelerated in reconnection region that we selected, which makes the index of the power-law spectrum increase.

In the range of $1 < \gamma_e < \gamma_0$, the power-law indexes of the electron spectrum driven by two lasers with MR (shown as the green dotted lines) are $p_1 = 1.4$, 1.8, and 1.9 in case A, B, and C, respectively shown in Figs. 4(a)–4(c). Compared with single laser driving case without MR, we find that MR amends the shape of the electron spectrum and makes the spectrum index p_1 less than 2 because more low-energy electrons are accelerated to higher energy in the MR process driven by two lasers. Moreover, with a decrease of the laser separation distance, the power-law spectrum is flattened. This is because the electron energy spectrum accelerated by lasers is flatter in the reconnection region when laser the separation distance increases. Meanwhile, the magnetic parameter σ of the background plasma before the MR is driven by lasers increases when the laser separation distance decreases (as shown in Table 1). Our simulation results agree with those of previous relativistic astrophysics research[32] in that the magnetic parameter affects electron acceleration in relativistic MR.

Table 1. Important parameters of the plasma environment.

Parameter	8 μm	9 μm	10 μm	Gamma ray bursts
System size (m)	10^{-5}	10^{-5}	10^{-5}	10^{4} [a]
Electron temperature (keV)	2.67	2.12	1.53	3×10^{2} [a]
Plasma density (cm^{-3})	1.15×10^{21}	1.15×10^{21}	1.15×10^{21}	2×10^{29} [a]
B_A (T)	1.97×10^{4}	1.45×10^{4}	1.06×10^{4}	4×10^{9} [a]
$\langle\beta\rangle$	0.1	0.2	0.7	1.1×10^{-3} [b]
$\langle\sigma\rangle$	24.43	15.56	13.01	3.0×10^{5} [b]
$(V_{Ae})_{max}$ (m/s)	2.8×10^{8}	2.5×10^{8}	2.3×10^{8}	2.0×10^{5} [b]
$(C_s)_i$ (m/s)	6.2×10^{5}	4.7×10^{5}	4.7×10^{5}	5.5×10^{6} [b]
$(C_s)_e$ (m/s)	2.17×10^{7}	1.94×10^{7}	1.64×10^{7}	–
v_{ms} (m/s)	2.8×10^{7}	2.5×10^{7}	2.3×10^{7}	–
v_d (m/s)	5.6×10^{7}	5.1×10^{7}	4.1×10^{7}	–
$(E_z)_{max}/E_0$	0.037	0.032	0.028	–
Reconnection rate	0.28	0.37	0.49	–

[a]Refs. [43,44]. [b]Our calculations.

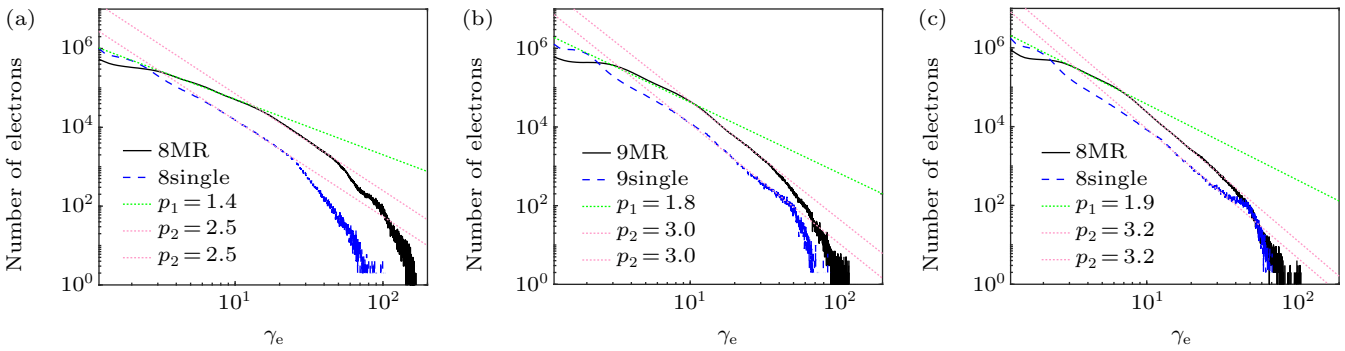


Fig. 4. The electron energy spectra for case A (a), B (b), and C (c) at the moment the maximum reconnection electric field is reached ($t = 50T_0$, $55T_0$, and $55T_0$, respectively). The vertical axis is the electron count, and the horizontal axis is the relativistic factor of electron. The solid line is for the two-laser case, and the dashed line is for the single laser. The electron distribution is fitted with the power-law spectrum $N(\gamma) = \gamma^{-p}$. The dotted line is the power-law spectrum line with different powers. The green dotted line is fitted with the low-energy region, and the pink dotted line is fitted with the middle-energy region.

4. Collisionless shock acceleration and magnetic reconnection acceleration

Figures 3(a)–3(c) not only present the electron pick-up ring but also two electron jets along the p_y direction. In particular, in Figs. 3(b) and 3(e), the pick-up ring is not obvious, while the electron jets along the p_y direction are enhanced. On the whole, the electron jets along the p_y direction are obviously present in case C.

Next, the formation mechanism of the electron jets along the p_y direction will be analyzed. Figure 5(a) shows the typical structures of CS, the electron density and electromagnetic fields around the shock front when the shock is fully formed[36] $t = 50T_0$ in case C (at $y = 12$ μm, $z = 20$ μm). It is found that there are two regions of electron density accu-

mulation generated by the interaction of two lasers expelling plasmas. Setting n_1 as the downstream density at $x = 14$ μm, which is in the region between the two laser beams, and n_2 as the upstream density (peak density of Fig. 5(a)) at $x = 14.5$ μm, the density ratio obtained is $n_2/n_1 \approx 4$. Then we determined the fast magnetosonic speed $v_{ms} = \sqrt{c_s^2 + V_{Ae}^2}$, the ion sound speed $c_s = \sqrt{Zk_B T_e/m_i}$[37] and the electrons' downstream velocity v_d in Table 1. Collisionless shock wave characteristics of $v_d > v_{ms}$ were found in this environment. The electric field E_x peaks around the wave front ($x = 14.5$ μm), providing electrostatic cross shock potential for capturing and reflecting electrons slower than the shock. Therefore, the shock wave can be formed between the laser beams, and the electrons should be accelerated in the shock front located in region I of Fig. 5(a), which is selected as 14 μm $< x <$ 14.5 μm, 11 μm $< y <$ 13 μm, and 10 μm $< z <$ 25 μm, as shown in the black dotted line rectangle on the bottom of Fig. 2(g). In order to compare with region I, region II of Fig. 5(a) is defined as an MR dominant region because this region is closer to the reconnection X-point, and it includes 14.5 μm $< x <$ 15 μm, 11 μm $< y <$ 13 μm, and 10 μm $< z <$ 25 μm in the black dotted line rectangle on the top of Fig. 2(g).

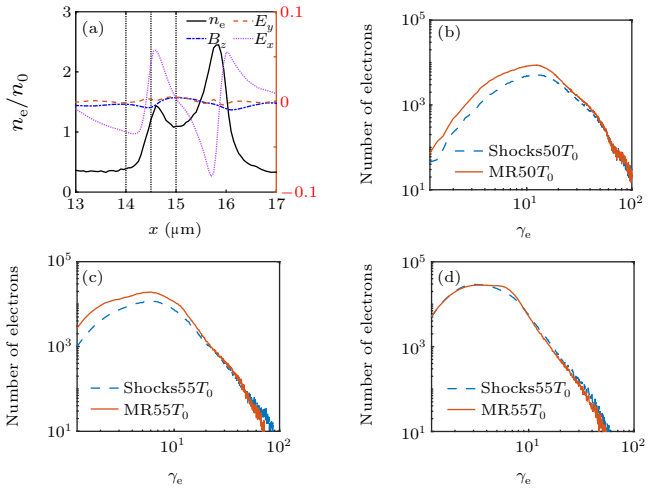


Fig. 5. Internal structure of a pair of CS at $t = 50T_0$ in case C. (a) Line out of the electron density (n_e; solid black line) and electromagnetic fields (B_z indicated by the blue dash-dotted line; E_y, red dashed line; E_x, purple dotted line), at $y = 12$ μm and $z = 20$ μm, region I from $x = 14$ μm to 14.5 μm and region II from $x = 14.5$ μm to 15 μm. The electron energy spectra for different acceleration mechanisms by CS (the blue dashed line) and MR (the red solid line) are in case A at $t = 50T_0$ (b), case B at $t = 55T_0$ (c) and case C at $t = 55T_0$ (d).

Figures 5(b)–5(d) show the electron energy spectrum in region I (blue dashed line) and region II (red line). Figure 5(b) shows that in case A, electrons are accelerated more in MR than in CS. As seen in Figs. 5(c) and 5(d), with increasing separation distance, the electron energy spectrum from CS approaches that from MR. This is because the enlarging separation distance between the two laser spots leads to amplification of the interaction region of the plasma generated by the two lasers. Collisionless shock wave survival time increases in this interaction region, which allows more electrons to be captured and accelerated by the collisionless shock.[38,39]

To explain the electron acceleration process, the temporal evolution of the electron kinetic energy (E_k) and the work done by each electric field component ($W_x = 0.5\varepsilon_0 E_x^2$, $W_y = 0.5\varepsilon_0 E_y^2$, and $W_z = 0.5\varepsilon_0 E_z^2$) for one typical electron are given for case A, case B, and case C in Fig. 6. W_x is related to the collisionless shock acceleration as shown by Lorenzo Sironi and Anatoly Spitkovsky;[39] W_z is the reconnection electric field contribution, W_y is the outflow direction and it should respond to the magnetic field effect (magnetic field compression, magnetic field betatron acceleration).[21]

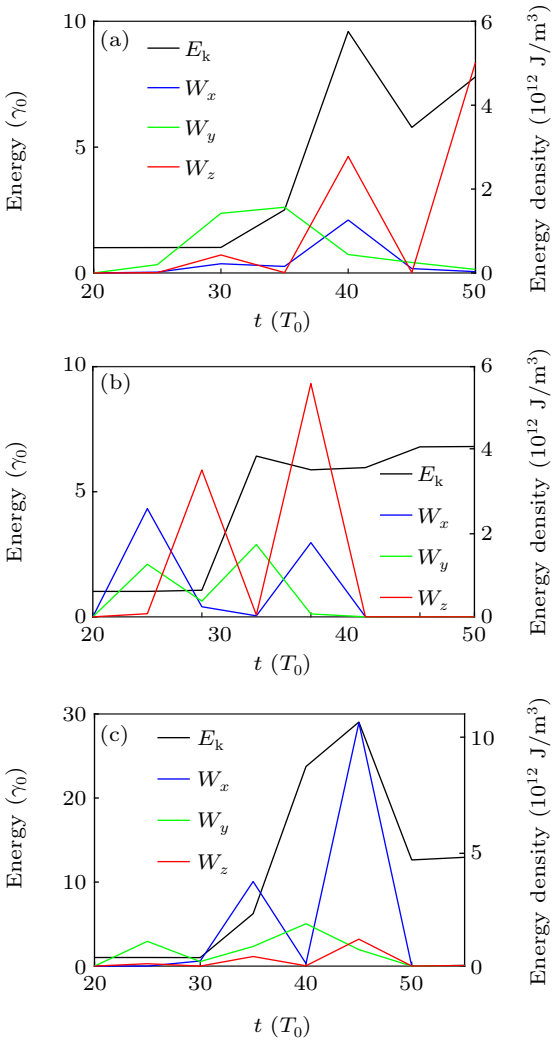


Fig. 6. Evolution of electron kinetic energy over time. The work done by each electric field component (W_x, W_y, W_z) is plotted for case A, B, and C in panels (a), (b), and (c).

Figure 6 shows that the electric fields E_x and E_z all play important roles in electron acceleration for case A, case B, and case C. In Fig. 6(a), for case A, the electron kinetic energy E_k mainly comes from W_x and W_z. The reconnection contribution is more than others. Figure 6(c) shows that some particles gained energy by W_x, and reconnection has less influence in case C. Therefore, figure 6 implies the results of Figs. 5(b)–

5(d), where more electrons are accelerated by collisionless shock when two magnetic tubes compress each other.

5. The 3D effects

In order to analyze some quantities, the 2D figures in the reconnection plane are presented, which are averaged along the z direction. This method may lead to the absence of some three-dimensional information. In Figs. 7(a)–7(c), the 3D isosurface distribution of the electron momentum p_y is presented for case A at $t = 50T_0$, and case B and case C at $t = 55T_0$, respectively. High-energy electrons are distributed at the front of the laser transmission channel. In contrast, in case A, electrons are concentrated in the reconnected region with a very narrow x scope, while in case B and case C, more energetic electrons along the y direction are located over the whole interaction region of the plasma generated by the two lasers, which means that more energetic electrons are located over a wider range of x. These features also imply that the acceleration mechanism is different.

According to the location of the outflow in the 3D scenario of Figs. 7(a)–7(c), the electron energy spectra are given in Figs. 7(d)–7(f) where the selected region is 13 μm $< x <$ 17 μm, 5 μm $< y <$ 19 μm, and 25 μm $< z <$ 40 μm where the outflows are located. We find that one part of the energy spectrum for the two lasers with MR is the same as the case of the single laser without MR; the other part of the electron energy spectrum is modified by MR, which can be fit as a power-law distribution and its index is close to 1. Re-calculating the magnetization parameter σ, they are 70.2, 38.8, and 37.7 in case A, case B, and case C, respectively. This plasma environment is ultra-relativistic, which results in a very flat electron energy spectrum.

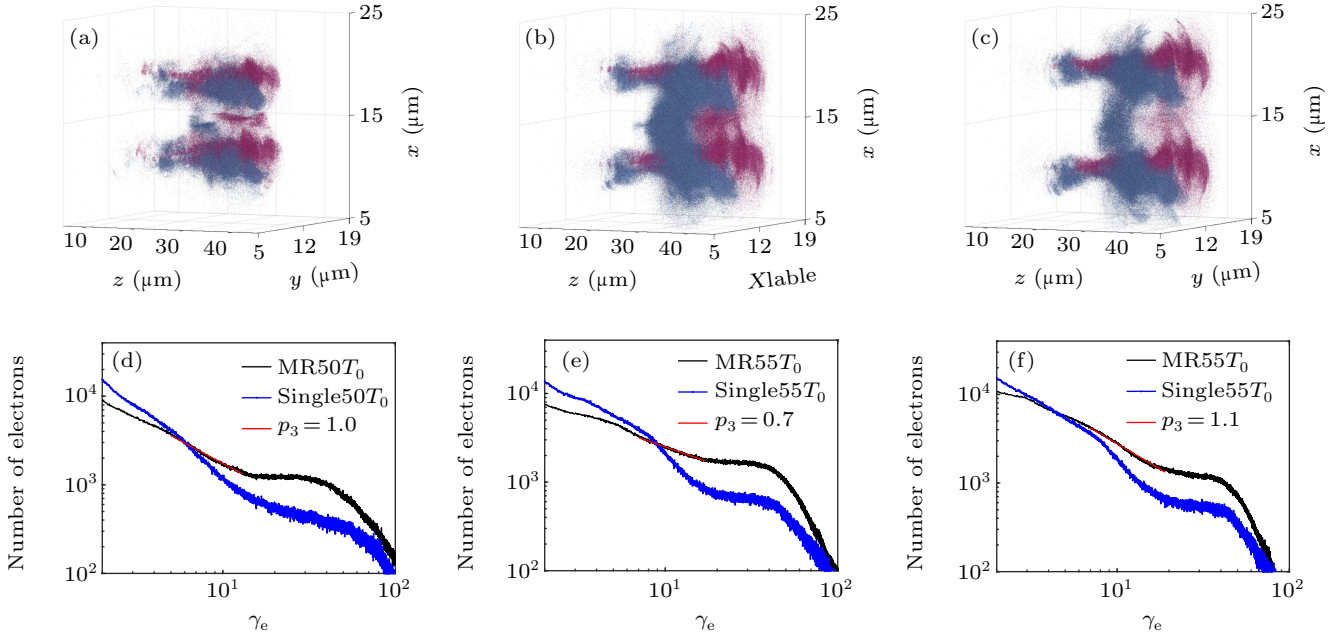


Fig. 7. (a)–(c) Three-dimensional isosurface distributions of the electron momentum p_y for case A, B, and C are at $t = 50T_0$ (a), $55T_0$ (b), and $55T_0$ (c), respectively. Here, purple shows along positive p_y and blue shows along negative p_y. (d)–(f) The corresponding two-laser case spectra (black lines) and the single-laser case spectra (blue lines) in the contrast diagram are also drawn for the electrons in the reconnection area ($x = 13$ μm–17 μm, $y = 5$ μm–19 μm, $z = 25$ μm–40 μm). The red lines indicate the power law of the spectrum $1 < \gamma_e < \gamma_0$.

6. Discussion and conclusions

Table 1 presents some parameters of the plasma environment driven by two ultra-intense femtosecond lasers and in a gamma ray burst environment. The σ is also much greater than unity $\sigma \geq 1$, and the energy density of the reconnection magnetic field is larger than the rest mass energy density of the electrons. Therefore, the MR driven by ultra-intense lasers is ultra-relativistic.

The plasma beta $\beta = 2\mu_0 n_e k_B T/B^2$ (β is the ratio of the thermal pressure to the magnetic pressure) is much smaller than 1. We find that the electron Alfvén speed is close to the speed of light $v_{Ae} \sim c$. These parameters match the environment of high-energy astronomical phenomena. Even though our simulation parameters do not exactly match high-energy astronomical ones, such as particle density, magnetic field energy, spatial and temporal scale, to some extent, our simulations reflect the mechanism and process of electron acceleration, corresponding to many high-energy emission of the astronomical observations.[40–42]

In this paper, from the momentum diagram, the "pick-up ring" shrinks as the laser separation distance increases. Fewer reconnection electric fields accelerate fewer electrons to higher energies. At the same time, two momentum jets along p_y are presented, and they are more obvious with an increase of the separation distance. This may be related with

the different acceleration mechanisms in the case with a different separation distance. With the increase of the laser separation distance, the binding of electrons in the magnetic field becomes weaker, the duration of CS becomes longer, and the acceleration space becomes larger. So, more electrons can be accelerated by CS. Therefore, in the p_y direction of the electron momentum phase space, jets appear and become larger as the laser separation distance increases. Then, through the energy spectrum analysis of different regions, we find that, with separation distance increasing, the electron energy spectrum of energetic electrons from collisionless shock approaches that from MR. As the separation distance decreases, the magnetization parameter σ increases, and the electron energy spectrum becomes flatter and less than 1. From the 3D momentum configuration, the outflow is presented between two lasers. According to the position of the outflow, the electron energy spectrum and the magnetization parameter are re-examined. The magnetization parameter is higher, and the index of the energetic electron spectrum is close to 1.

Acknowledgments

This work was supported by the National Natural Science Foundation of China (Grant Nos. U1930108,12175018, 12135001, 12075030, and 11903006) and the Strategic Priority Research Program of the Chinese Academy of Sciences (Grant No. XDA25030700). Yongli Ping acknowledges the support of the Open Research Program from Key Laboratory of Geospace Environment CAS.

References

[1] Ghisellini G, Celotti A and Lazzati D 2000 *Mon. Not. R. Astron. Soc.* **313** L1
[2] Lesch H and Birk G T 1998 *Astrophys. J.* **499** 167
[3] Reames D V 2013 *Space. Sci. Rev.* **175** 53
[4] Berezhko E G and Ksenofontov L 1999 *J. Exp. Theor. Phys.* **89** 391
[5] Meli A and Quenby J J 2003 *Astropart. Phys.* **19** 649
[6] Kinney R and McWilliams J C 1995 *Small-Scale Structures in Three-Dimensional Hydrodynamic and Magnetohydrodynamic Turbulence* **462** 289
[7] Li C K, Séguin F H, Frenje J A, Rygg J R, Petrasso R D, Town R P J, Landen O L, Knauer J P and Smalyuk V A 2007 *Phys. Rev. Lett.* **99** 055001
[8] Palmer C A J, Campbell P T, Ma Y, Antonelli L, Bott A F A, Gregori G, Halliday J, Katzir Y, Kordell P, Krushelnick K, Lebedev S V, Montgomery E, Notley M, Carroll D C, Ridgers C P, Schekochihin A A, Streeter M J V, Thomas A G R, Tubman E R, Woolsey N and Willingale L 2019 *Phys. Plasmas* **26** 083109
[9] Nilson P M, Willingale L, Kaluza M C, Kamperidis, C, Minardi S, Wei M S, Fernandes P, Notley M, Bandyopadhyay S, Sherlock M, Kingham R J, Tatarakis M, Najmudin Z, Rozmus W, Evans R G, Haines M G, Dangor A E and Krushelnick K 2006 *Phys. Rev. Lett.* **97** 255001
[10] Dong Q L, Wang S J, Lu Q M, Huang C, Yuan D W, Liu X, Lin X X, Li Y T, Wei H G, Zhong J Y, Shi J R, Jiang S E, Ding Y K, Jiang B B, Du K, He X T, Yu M Y, Liu C S, Wang S, Tang Y J, Zhu J Q, Zhao G, Sheng Z M and Zhang J 2012 *Phys. Rev. Lett.* **108** 215001
[11] Zhong J, Li Y, Wang X, Wang J, Dong Q, Xiao C, Wang S, Liu X, Zhang L, An L, Wang F, Zhu J, Gu Y, He X, Zhao G and Zhang J 2010 *Nat. Phys.* **6** 984
[12] Kuramitsu Y, Chu H H, Hau L N, Chen S H, Liu Y L, Hsieh C Y, Sakawa Y, Hideaki T and Wang J 2015 *High. Energy. Density. Phys.* **17** 198
[13] Zhong J Y, Lin J, Li Y T, Wang X, Li Y, Zhang K, Yuan D W, Ping Y L, Wei H G, Wang J Q, Su L N, Li F, Han B, Liao G Q, Yin C L, Fang Y, Yuan X, Wang C, Sun J R, Liang G Y, Wang F L, Ding Y K, He X T, Zhu J Q, Sheng Z M, Li G, Zhao G and Zhang J 2016 *Astrophys. J. Suppl. Ser.* **225** 30
[14] Fox W, Park J, Deng W, Fiksel G, Spitkovsky A and Bhattacharjee A 2017 *Phys. Plasmas* **24** 092901
[15] Raymond A E, Dong C F, McKelvey A, Zulick C, Alexander N, Bhattacharjee A, Campbell P T, Chen H, Chvykov V, Del Rio E, Fitzsimmons P, Fox W, Hou B, Maksimchuk A, Mileham C, Nees J, Nilson P M, Stoeckl C, Thomas A G R, Wei M S, Yanovsky V, Krushelnick K and Willingale L 2018 *Phys. Rev. E* **98** 043207
[16] Yi L, Shen B, Pukhov A and Fülöp T 2018 *Nat. Commun.* **9** 1601
[17] Law K F F, Abe Y, Morace A, Arikawa Y, Sakata S, Lee S, Matsuo K, Morita H, Ochiai Y, Liu C, Yogo A, Okamoto K, Golovin D, Ehret M, Ozaki T, Nakai M, Sentoku Y, Santos J J, d'Humières, E, Korneev P and Fujioka S 2020 *Phys. Rev. E* **102** 033202
[18] Fox W, Matteucci J, Moissard C, Schaeffer, D B, Bhattacharjee A, Germaschewski K and Hu S X 2018 *Phys. Plasmas* **25** 102106
[19] Fiuza F, Swadling G F, Grassi A, Rinderknecht H G, Higginson D P, Ryutov D D, Bruulsema C, Drake R P, Funk S, Glenzer S, Gregori G, Li C K, Pollock B B, Remington B A, Ross J S, Rozmus W, Sakawa Y, Spitkovsky A, Wilks S and Park H S 2020 *Nat. Phys.* **16** 916
[20] Lu S, Lu Q, Huang C, Dong Q, Zhu J, Sheng, Z, Wang S and Zhang J 2014 *New J. Phys.* **16** 083021
[21] Lu S, Lu Q, Guo F, Sheng Z, Wang H and Wang S 2016 *New J. Phys.* **18** 013051
[22] Qiao B, Xu Z, Yao W P, Chang H X and He X T 2017 *Plasma Phys. Control Fusion* **59** 064002
[23] Gu Y J, Pegoraro F, Sasorov P V, Golovin D, Yogo A, Korn G and Bulanov S V 2019 *Sci. Rep.* **9** 19462
[24] Ping Y L, Zhong J Y, Sheng Z M, Wang X G, Liu B, Li Y T, Yan X Q, He X T, Zhang J and Zhao G 2014 *Phys. Rev. E* **89** 031101
[25] Ping Y L, Zhong J Y, Wang X G, Sheng Z M and Zhao G 2017 *Astrophys. J.* **849** 137
[26] Bessho N and Bhattacharjee A 2012 *Astrophys. J.* **750** 129
[27] Guo F, Li X, Li H, Daughton W, Zhang B, Lloyd-Ronning N, Liu Y H, Zhang H and Deng W 2016 *Astrophys. J.* **818** L9
[28] Sironi L and Spitkovsky A 2014 *Astrophys. J.* **783** L21
[29] Hoshino M 2005 *J. Geophys. Res. Space. Phys.* **110** A10215
[30] Zenitani S and Hoshino M 2007 *Astrophys. J.* **670** 702
[31] Dahlin J T 2020 *Phys. Plasmas* **27** 100601
[32] Lu Y, Guo F, Kilian P, Li H, Huang C and Liang E 2021 *Astrophys. J.* **908** 147
[33] Yan X Q, Lin C, Sheng Z M, Guo Z Y, Liu B C, Lu Y R, Fang J X and Chen J E 2008 *Phys. Rev. Lett.* **100** 135003
[34] Liu B, Wang H Y, Liu J, Fu L B, Xu Y J, Yan X Q and He X T 2013 *Phys. Rev. Lett.* **110** 045002
[35] Ping Y L, Zhong J Y, Wang X G, Zhao G, Li Y T and He X T 2021 *Plasma Phys. Controlled Fusion* **63** 085012
[36] Yao W, Fazzini A, Chen, S N, Burdonov K, Antici P, Béard J, Bolaños S, Ciardi A, Diab R, Filippov E D, Kisyov S, Lelasseux V, Miceli M, Moreno Q, Nastasa V, Orlando S, Pikuz S, Popescu D C, Revet G, Ribeyre X, d'Humières E and Fuchs J 2020 *Nat. Phys.* **17** 1177
[37] Fiuza F, Fonseca R A, Tonge J, Mori W B and Silva L O 2012 *Phys. Rev. Lett.* **108** 235004
[38] Spitkovsky A 2008 *Astrophys. J.* **682** L5
[39] Sironi L and Spitkovsky A 2011 *Astrophys. J.* **726** 75
[40] Celotti A and Ghisellini G 2008 *Mon. Not. R. Astron. Soc.* **385** 283
[41] Zhang B and Yan H 2011 *Astrophys. J.* **726** 90
[42] Zhang J, Liang E W, Sun, X N, Zhang B, Lu Y and Zhang S N 2013 *Astrophys. J.* **774** L5
[43] Ji H and Daughton W 2011 *Phys. Plasmas* **18** 111207
[44] Uzdensky D A 2011 *Space Sci. Rev.* **160** 45